Rapid L-PBF printing of IN718 coupled with HIP-quench: A novel approach to manufacture and heat treatment of a nickel-based alloy

(Article begins on next page)
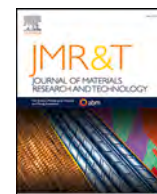
19 November 2024

Rapid L-PBF printing of IN718 coupled with HIP-quench: A novel approach to manufacture and heat treatment of a nickel-based alloy

S. Lerda [a,b], E. Bassini [a,b,c,*], G. Marchese [a,b,c], S. Biamino [a,b,c], D. Ugues [a,b,c]

[a] DISAT – Department of Applied Science and Technology, Politecnico di Torino, Corso Duca Degli Abruzzi 24, 10129, Torino, Italy
[b] IAM@PoliTo – Interdepartmental Center of Integrated Additive Manufacturing, Politecnico di Torino, Corso Castelfidardo 51, 10129, Torino, Italy
[c] INSTM - Consorzio Interuniversitario Nazionale per La Scienza e Tecnologia Dei Materiali, Via G. Giusti 9, 50121, Firenze, Italy

ARTICLE INFO

Handling Editor: P Rios

ABSTRACT

There has been a growing interest in additive manufacturing in recent years, with researchers actively working on improving component quality through adjustments to printing parameters, lead time, and productivity. Rapid L-PBF printing has emerged as an attractive approach to expedite component manufacturing. However, employing a rapid building strategy may lead to additional internal flaws, which can be addressed during a Hot Isostatic Pressing (HIP) cycle. In this study, Inconel 718 was L-PBF printed using two distinct strategies: one involving the creation of a dense 1 mm shell with loosely packed powders in the core and the other utilizing different sets of printing parameters for the shell and core, respectively. These strategies resulted in a 60% and 45% printing time reduction, respectively, compared with the time requirement for printing same-size cubic samples with optimized parameters. Additionally, full densification and porosity elimination were achieved through a HIP-quench approach, obviating the need for further heat treatment. The study presents the final microstructures and retained flaws, along with assessing the degree of recrystallization via EBSD analysis and evaluating mechanical properties using hardness measurements and compression tests.

1. Introduction

Additive Manufacturing (AM) is becoming increasingly frequent for producing structural components in the automotive, medical, and aerospace fields [1,2]. Laser powder bed fusion (L-PBF) is among the most used AM techniques and is typically adopted when a component with a complex design must be manufactured [3,4]. AM techniques become extremely handy when standard components must be optimized for weight reduction, such as after applying topological optimization algorithms [5]. Furthermore, the considerable design freedom of AM allows for limiting the number of joints and welds, obtaining a further weight reduction [6].

The performance of an L-PBF component is strongly related to the defect density left after the printing stage. Pores, lack of fusion, or cracks can populate the sample even after an in-depth parameter optimization [7]. The nature and origin of these defects were thoroughly discussed in the literature, as their adverse effects against quasi-static and cyclic mechanical properties [8]. Apart from the defects, the microstructure of AM components is another important topic. The continuous interaction between the laser and the printed layers develops a microstructure different from those obtained with traditional means such as casting or wrought. The fast-cooling rate and the complex heat flux towards the building platform generate a very fine microstructure with elongated grains along the building direction [9]. The above-mentioned inhomogeneity and anisotropy can be removed after tailoring the process parameters and performing adequate heat treatments and post-processing [10,11].

Despite all these operations, AM components can still be deficient compared to traditional manufacturing methods, especially when fatigue resistance is concerned. Unexpected flaws within the material could act as crack initiators, undermining the overall behavior of the samples. Hot isostatic pressing (HIP) can be introduced as a further post-processing step, especially in all those critical fields where the zero-flaw policy applies, such as in the aeronautical one [12–18]. Newly developed HIP facilities can close submerged defects by applying heat and high pressures (above 100 MPa) through an inert gas (normally Argon) and delivering full heat treatments with a controlled cooling rate. This possibility is desirable because it enhances the material's final mechanical properties by eliminating the flaws and getting the most suitable microstructure, with considerable time-saving. From a

---

microstructural perspective, as shown by Sadeghi et al. [19], controlling the cooling rate after HIP is important to avoid excessive grain coarsening and the detrimental formation of the δ phase at the grain boundaries in the IN718. HIP positive effects are mostly known when fatigue resistance is involved. The closure or the size reduction of pores, cracks, and lack of fusion immediately leads to an increase in the fatigue limit of HIPped materials and a reduction in the experimental data's scattering [20]. However, it is important to mention that only deep and enclosed defects can be mitigated. All cracks, pores, or similar discontinuities interconnected to the sample's surface will be filled with Ar, balancing the applied isostatic pressure. This fact impedes the closure of superficial defects, which remain unaltered. Based on these considerations, it becomes progressively more interesting to modify the printing strategies to obtain a fully dense shell of material embedding a portion where printing parameters could dramatically change. A possible strategy is to print the inner part of the material with very fast scanning speeds, increasing the overall number of internal defects but considerably reducing the printing times. These defects could be healed during post-processing with HIP. Changing the printing strategies between the shell and the inner part is fundamental because interconnected defects with the surface will make the HIP process useless, especially when extensive defects are present [21]. Others, such as [22,23], have suggested embedding loosened powders directly during the L-PBF process, producing the shell with optimized printing parameters. This process can effectively produce densified components but suffer significant shrinkage during densification. This aspect is particularly intensified due to the narrow PSD of the L-PBF powders. Thus, it must be balanced during the design stage, optimizing the CAD model using models and simulations [24]. Another possible problem with this procedure is the formation of prior particle boundaries (PPBs) at the consolidated powder surface. One of the main concerns with these particles is the severe reduction in ductility they cause, especially when present in high-volume fractions, such as in powders containing high oxygen levels [25].

Many authors reported the PPBs problem in the literature for IN718. Kuo et al. [26] reported lower ductility during high-temperature tensile tests. Nevertheless, some studies were performed to mitigate this condition. For instance, Chang et al. tailored the HIP temperature of IN718 to limit PPB presence by treating the sample in a super-solidus regime (at 1275 °C) for a short time [27]. More specifically, the authors suggest performing the HIP treatment at least at 1150 °C and with a pressure higher than 150 MPa to reduce pores and defects in L-PBF samples significantly.

The shelling method is a hybrid technique that combines the design freedom of additive manufacturing with the densification capability of the HIP. In particular, the primary benefit of using the HIP immediately after AM consists of achieving the complete densification of the component where one could deliberately increase the number of defects, for example, increasing the printing speed, which is notoriously relatively slow in conventional printing. The shelling method drastically reduces the printing time by limiting the laser interaction with the powders only at the outer shell without processing the entire component volume. It was proved by several works in the literature that the tensile properties of shelled components are close to those observed in traditional L-PBF components after HIP and heat treatment for materials other than Ni alloys [22,28–33]. The current paper investigates how samples printed with different strategies behave when subjected to strong compression stress. Even if this type of solicitation is less demanding than a tensile test, plastic deformation can be easily observed, and any detachment of the grains during their sliding can be detected. This work focuses mainly on the adverse effects of the (PPBs) during plastic deformation and proposes a printing procedure to reduce the lead time by limiting the negative effect of the presence of PPBs. At the same time, the use of controlled cooling after HIP allowed further time savings by eliminating the need for solution annealing. Furthermore, this paper evidence how the shelling and controlled porosity

techniques coupled with Hot Isostatic Pressing could introduce time reductions in two distinct point of the process: the first is at the printing stage, here, printing time is reduced by 60 and 45% respectively, compared with the time required to print a dense cubic sample with optimized printing parameters. The second time saving comes from the elimination of a dedicated annealing heat treatment in a low-pressure furnace for the Ni-based alloy. This step is accomplished by means of HIP quench where healing and heat treatment are performed at the same time.

2. Materials and methods

2.1. Inconel 718 powders

All the samples produced in this work were obtained from IN718 gas-atomized powders by EOS GmbH, whose chemical composition, according to its datasheet, is reported in Table 1.

2.2. The laser powder bed fusion (L-PBF) process

The samples were printed in a Concept Laser Mlab R (Concept Laser GmbH) equipped with an optical fiber laser with a power output of 100 W and a spot size of 50 μm. The building platform, a 90 mm square, was made of AISI 316 L stainless steel. Apart from three reference cubes obtained with standard printing parameters abbreviated as optimized parameters (OP), the samples used in this work were produced with two main printing strategies. The first consisted of printing 3 cubes using optimized parameters just for the outer shell, leaving the remaining powders inside unaltered and loosened, which are now referred to as *shelled samples* (SS). In these samples, the shells were printed using the parameter set 1 of Table 2. The second consisted of printing the samples with two sets of parameters: the inner part was printed with a faster scan speed, i.e., 2400 mm/s (parameter set 2 of Table 2), while the shells were printed with the standard scanning speed of 800 mm/s (i.e. parameter set 1 Table 2). This mixed printing condition allowed a significative printing time reduction and samples with fully dense shells and a core with a higher density of printing defects. These samples are referred to as "*controlled porosity*" (CP). As mentioned above, Table 2 shows the main printing parameters for reference.

All the samples were printed using a 5 mm stripes strategy and a laser beam rotation of 67° among each layer, reducing the residual stress and creating a less inhomogeneous microstructure [34].

Fig. 1 shows the CAD drawing used in this work to build the SS and the CP samples. More specifically, the grey part represents the volume printed with optimized parameters and a slow scan speed, i.e., the shell. Conversely, the yellow volume can be printed using the high scan speed or a portion filled with un-melted powders. The dome structure was inspired by the work of Du Plessis et al. [33] and optimized to be self-sustaining. The changes aim to avoid any delamination among the layers without the need for printing any support. This condition was accomplished by controlling the dome's geometry, more specifically, its vertical tangent was limited to a 30° angle with respect to the Z direction.

The vertical wall thickness is 1 mm, while the portion in contact with the building plate is 2 mm thick. Some overstock material helped during the sample's electro-discharge machining (EDM) cut, which was performed exactly 1 mm above the platform, leading to a uniform shell thickness. In the dome portion, the shell thickness is not constant and ranges between 1.0 and 2.3 mm referred to in the z direction. Eventually, a different type of sample was built for compression testing consisting of cylinders with a diameter of 10 mm and 16 mm of height. The same building strategies described above were used to print two cylinders families. At the same time, a third type of cylinder, built with optimized L-PBF parameters, was built and used as a benchmark. The first two-cylinder types were then machined down to a diameter of 8 mm and height of 14 mm to eliminate the shell and test only the portion of

Table 1
Chemical composition of used IN718 powders.

Element	Ni	Fe	Cr	Nb	Mo	Ti	Al	Co	Cu	Si	Mn	C
wt.%	52.5	Bal.	19	5.125	3.05	0.9	0.5	0.5	0.15	0.175	0.175	0.04

Table 2
Parameters sets used during the L-PBF printing stage.

Parameter set	Laser Power [W]	Layer thickness [µm]	Scanning speed [mm/s]	Hatching Distance [mm]
1	95.00	20.00	800.00	0.05
2	95.00	20.00	2400.00	0.05

material obtained with the faster strategies. Fig. 2 shows a schematic of the cylinders used for the compression test. A flat side was machined and mirror-polished to observe the deformed microstructure immediately after the compression test, as suggested by Martelli et al. [35].

2.3. Hot Isostatic Pressing (HIP) and heat treatment

The Hot Isostatic Pressing treatment was performed in a Quintus *QIH 15L* (by Quintus Technologies AB) equipped with a molybdenum furnace and the Uniform Rapid Cooling (URC) module, which can cool the sample after HIP at a maximum rate of 294 °C/min. The system has a maximum operating temperature of 1400 °C and a maximum pressure of 210 MPa using Argon as operating media. Using the URC module, HIP was used to densify the samples and perform the solution annealing. The HIP-Annealing (HIP-A) temperature was 1200 °C with a heating rate of 10 °C/min, the soaking time of 4 h, and the applied pressure 170 MPa. After HIP-A, the fastest cooling rate achievable (294 °C/min measured between 1200 and 400 °C with a thermocouple in closed contact with the sample) was applied to suppress the formation of any brittle face such as Topological Closed Packed (TCP) or Laves phases [36].

2.4. Sample density assessment

Sample density was determined right after the L-PBF process and after HIP-A. The apparent density of as-built samples was measured with a gas pycnometer *Ultrapyc 5000* by Anton Paar, using He with a 2 bar pressure, calibrated with a steel sphere with known volume and density. The number of measurements changes, aiming for a standard deviation smaller than 0.05 % during the last three repetitions. After densification with HIP, the density was measured with the pycnometer and via image analysis to double-check the results. The analysis was performed by cutting the samples in half; the surfaces were then ground with SiC

papers and polished with diamond pastes. The final surface finishing was obtained using a water-based colloidal silica solution. Each surface was observed with a light optical microscope, taking 12 pictures at 50× magnification. The micrographs were then processed via the image recognition software ImageJ.

2.5. Sample shape reconstruction after HIP and deformation assessment

The deformation of the samples induced by the densification after the HIP-A was assessed with a touch profilometer Mahr *CD12*0 by
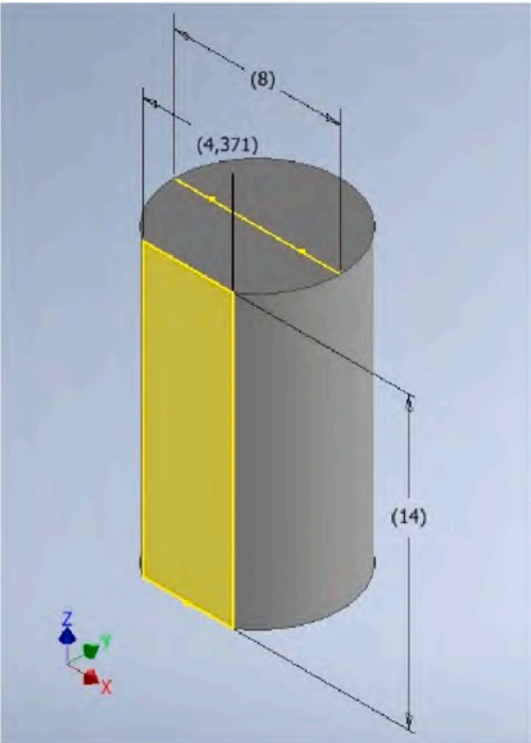
Fig. 2. 3D schematic of the cylinder used for compression test. The flat surface was used to observe plastic deformation directly from the mechanical test.
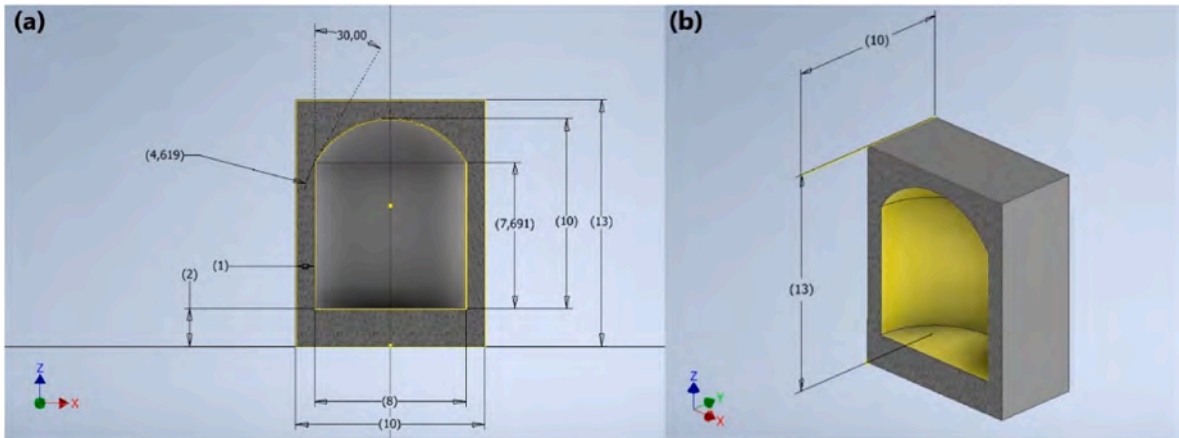
Fig. 1. Graphic representation of printed samples' cross sections in 2 d (a) and 3 d (b). The figure shows the most relevant dimensions of the samples.

MarSurf after receiving a sandblast cycle to reduce the friction between the surfaces and the profilometer tip. The measurement was performed three times along the centerline, searching for the maximum displacement from the original CAD model.

2.6. Sample preparation for microstructural assessment

The metallurgical preparation was similar to that used to determine the residual porosity. More specifically, after polishing, the microstructural features were revealed using an electrolytic etching applying 3 V for 5 s and a solution of 15 ml HCl and 5 ml HNO$_3$. The resulting microstructures were observed with an optical microscope, a Leica MEF4, and a scanning electron microscope, Zeiss EVO 15, equipped with an EDS probe Ultim-max by Oxford instruments. Electron backscattered diffraction (EBSD) assessment was performed in a Tescan S900G FESEM to appreciate better how the printing strategies alter the grain morphology.

2.7. Micro-hardness test

The micro-hardness test was performed using a Leica VMHT with a load of 200 g (HV0.2) following the UNI-EN-ISO 6507-1. After a calibration step, indentations were performed along the building direction on the reference AB OP and the HIPed conditions to evaluate how hardness changes across the shell-core interface layer.

2.8. Compression tests on cylinders

A compressive test was performed using a Zwick-Roell Z100 universal tensile machine equipped with a 100 kN loading cell to appreciate the differences between the two printing strategies. The force was applied with a constant rate up to the maximum applicable load on the samples shown in Fig. 2. The material underwent a severe deformation but never failed under the applied load. As described above, a flat face parallel to the building direction was mirror polished and used to observe grain deformation and sliding during the compression test.

3. Result and discussion

3.1. Powder

Powders were assessed in their cross-sections to observe their microstructure and investigate the internal defects. The results are shown in Fig. 3.

Fig. 3 a) shows the etched cross-section of an IN718 powder particle. The internal microstructure consisted of a fine dendritic structure with evident segregations during the rapid solidification in the gas atomization process [37]. At the same time, Fig. 3 b) highlights some internal spherical pores randomly distributed in the powder. The inert gas of the atomization caused the formation of this defect, which was trapped in the molten metal droplets during the process [38]. These spherical

defects are likely to be overturned by the fast melting and solidification of the L-PBF process. On the other hand, this defect could limit a sample's overall density when densification is obtained via solid-state diffusion. Nevertheless, HIP, thanks to the high pressure applied, is known to broadly limit this effect, providing a nearly fully dense product [39].

3.2. Densification

Fig. 4 a) summarizes the density levels achieved before and after the HIP process.

The density values are plotted as a function of the samples and conditions investigated. In addition, the residual porosity values were evaluated by cross-section image analyses on AB OP, HIP OP, SS, and CP. This analysis was performed to double-check the density values obtained, primarily because pycnometer analyses likely neglect the smallest defects.

AB OP density level of 8.23 g/cm^3 remained almost constant after the HIP process. Meanwhile, the residual porosity was reduced from 0.04% to 0.02%. The AB OP density value was already close to the theoretical density for traditionally processed IN718, justifying the negligible macroscopic density increment after HIP. Micrometrical and sub-
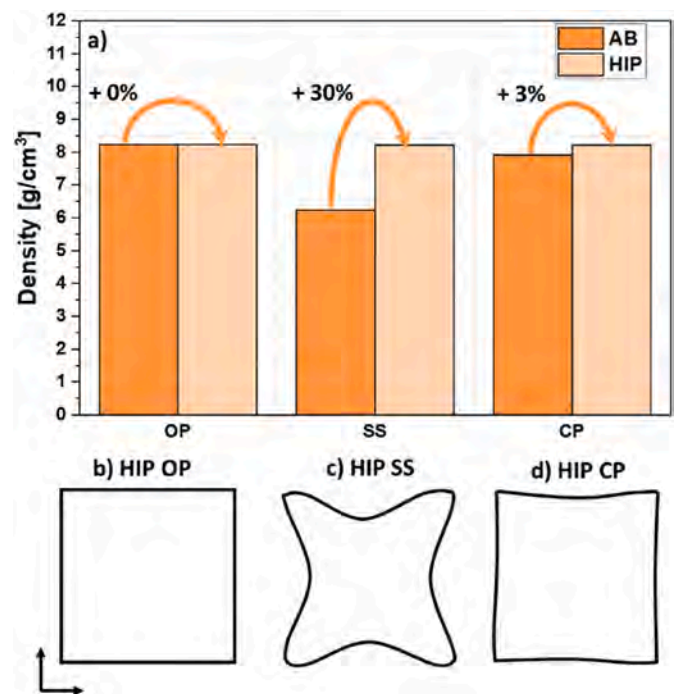

Fig. 4. a) Density results of OP, SS and CP samples before and after HIP Shrinkage patterns of b) HIP OP, c) SS and d) CP samples.
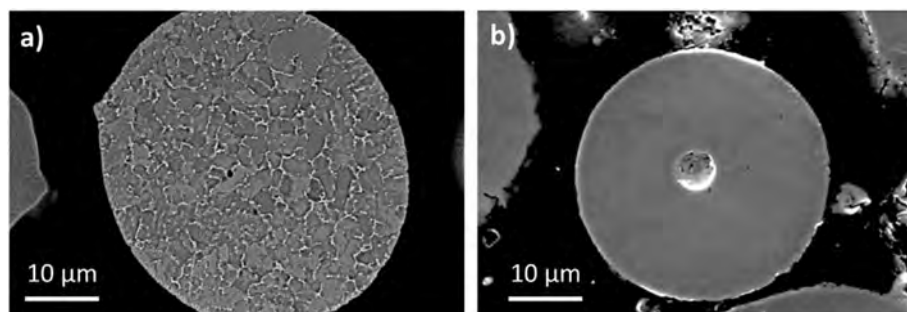

Fig. 3. a) Powder microstructure cross-section b) Defects in powder cross-section.

micrometrical spherical defects were healed or fully collapsed after HIP, revealing the expected densification behavior [40].

SS sample density increased from 6.25 g/cm^3 in the AB condition to 8.22 g/cm^3 in the HIPed one with a residual porosity of 0.03%. The HIP SS density value was close to the HIP OP reference value of 8.23 g/cm^3 reported in the previous paragraph. Together with the density tests, the apparent density of loosened powder inside the shelled samples was calculated and evaluated at 52.36% for the AB SS condition. According to the literature [41], this value fits with the theoretical 50 % powder bed density given by Additive Manufacturing techniques. Indeed, the apparent density of 52.36% is lower than the desired tap density values requested for the HIP process (63%–65%) [42]. This condition originated from the narrow PSD of L-PBF powders, which drastically reduced the initial tap density of the sample. Anyhow, the residual porosity of the HIP SS sample suggested a positive response to the HIP process.

AB CP density after the HIP process raised from 7.92 g/cm^3 (AB CP) to 8.21 g/cm^3 (HIP CP) with a residual porosity of the HIPed sample of 0.01%. In other words, the achieved density fell between the AB OP and SS conditions. The final HIPed CP sample density was comparable with the reference HIPed OP and the HIPed SS. Moreover, residual porosity indicates a good densification behavior of the highly porous core.

Fig. 4 b), c), and d) summarize the HIPed OP, SS, and CP sample shrinkage patterns. More specifically, HIPed OP did not undergo shrinkage compared to the AB, in accordance with the macroscopical 0% densification after HIP. Furthermore, HIPed SS exhibited the most significant shrinkage compared to the other conditions, resulting in a maximum mean deformation of 1.32 mm in the xy plane. This behavior is directly related to the PSD of the loosened powder used during the printing phase. HIPed CP sample represented the best compromise. The shrinkage pattern underlined a negligible shrinkage along the x-axis, and the mean maximum deformation of the y-axis direction was 0.20 mm. The CP strategy combined with the HIP process allowed the achievement of a final dense product with negligible shrinkage, significantly reducing the overall building time compared with the OP sample. The different shrinkage behaviors can be summarized in Fig. 5, which shows a reconstruction of the entire sample cross-section and allows to observe the deformation achieved in the samples after HIP.

Fig. 5 a) and b) report the OM cross-sectional images of CP and HIP SS, respectively. In the HIP SS sample, the difference between the shell and the core is evident due to the difference in grain size between the two areas. Specifically, the external part shows coarser grains, while finer ones were observed in the core section, showing features more similar to that of a sintered products [17,18].

3.3. Microstructural evolution

This section contains an in-depth description of the microstructural evolution of the samples after HIP post-processing. The analysis of the as-built L-PBF samples has the primary role of building a reference condition and finding any similarity across all the other microstructures described in the following sections.

Fig. 6 shows the microstructural evolution of the OP sample observed in AB and HIPed conditions. In particular, Fig. 6 a) and b) show an example of low and high-magnification images of AB OP sample. In contrast, Fig. 6 c) and d) represent the low and high magnification microstructure of HIP OP one.

AB OP sample shows a microstructure consisting of melt pools and columnar grains parallel to the building direction. Moreover, grains extend through several melt pools, thus confirming the epitaxial growth given by the partial remelting of previously built layers during the process. These microstructural features were consistent with other literature on the microstructural characterization of L-PBFed products [43,44]. Higher magnification, as shown in Fig. 6 b), confirmed the presence of melt pools and columnar grains and revealed a fine dendritic structure inside the grains. This feature was ascribed to the high cooling rates reached during the L-PBF process [45,46].

A consistent grain coarsening was observed in the HIPed OP, caused by the high temperature soaking at 1200 °C during the HIP treatment. However, the grains still show a preferential orientation that coincides with the building's direction, according to the evidence reported by Rezaei et al. [47]. SEM investigations of the HIP OP sample demonstrate the total dissolution of the dendritic structure inside grains and the formation of twinned boundaries. This microstructural evolution is strongly related to the HIP treatment performed above the traditional solution annealing for IN718 (1095 °C), which, however, promoted a general microstructural homogenization and limited the negative effect of PPBs [48]. These evidences were found in line with the literature; for instance, Cortes et al. [49] detected an increase in twin boundary formation during the HIP process above 1170 °C.

Fig. 7 compares the microstructure of the shelled samples in a central position. Depending on the adopted building strategy, grain size and morphology were significantly impacted.

More specifically, Fig. 7 a) shows the CP sample grain structure, characterized by equiaxed grains which were able to grow through PPBs particles with only a few exceptions, as depicted in the inset, showing sub-micrometric carbides and oxides at the interface between two adjoining grains. Conversely, Fig. 7 b) shows severe particle precipitation with many spherical particles, indicating that the grains could not grow beyond the powder boundaries, forming an almost continuous network of PPBs.
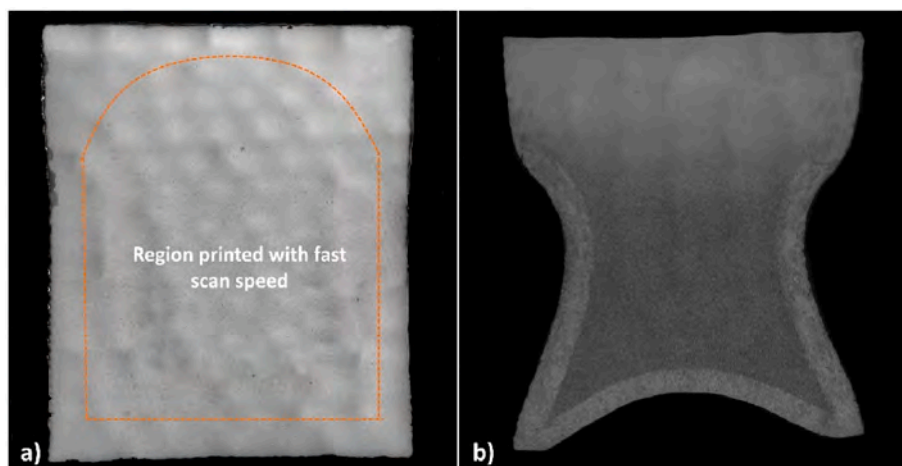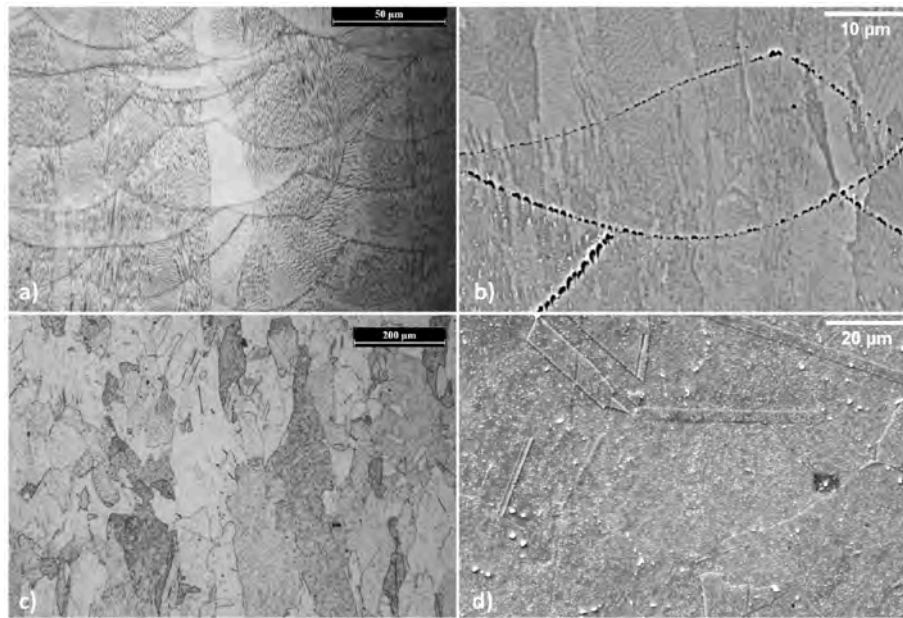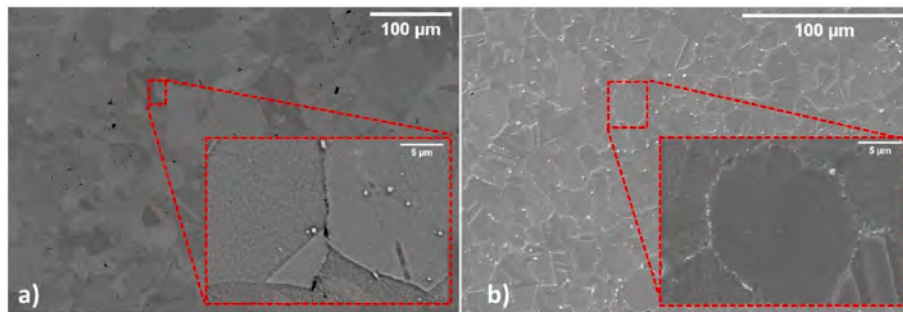

Fig. 5. Etched CP a) and SS b) cross-section.

Fig. 6. OM a) and SEM b) images of AB OP and HIP OP c) and d).

Fig. 7. Microstructure of the CP sample core a) and from the HIP OP b) the grain size and morphology are different, and a significant amount of PPBs can be observed.

Fig. 8 shows the chemical assessment of the particles described above. Fig. 8 a) and b) represent the CP and SS samples, respectively.

The eds spectra were taken on the matrix (solid colour) and the particles (red line). Regardless of the building technique adopted, the particles have a chemistry compatible with mixed carbides. This assumption can be concluded by observing the spectra showing higher peaks for the carbide former elements: Ti, Cr, Mo and Nb. These features comply with the theory that oxides formed on the top of powders act as preferential sites for the nucleation of carbides in later stages of the manufacturing process. The most evident difference between the two scenarios is that the CP sample shows the newly formed carbides randomly distributed throughout the matrix. Conversely, the SS sample has almost a continuous network of PPBs particles, which strongly hindered the grain growth within the sample core.

Fig. 9 focuses on the interface between the shell and the core of the samples. Again, the most noticeable difference between the two strategies is the total amount of particles formed in this specific portion of the samples. The SS sample shows almost a continuous film of carbides and oxides, which separates the shell from the core material. The CP sample, however, shows similar particles in this location, but their presence is significantly smaller, and they do not form a continuous layer. This difference can be explained by considering that the walls of the shell and the powders only had a limited interaction during the printing stage. At the same time, a strong solid-state diffusion took place during HIP, which could have helped this intense particle precipitation.

Conversely, in the CP sample, the shell and the core were intimately bonded during the printing due to the laser's repeated melting and solidification phases. At the same time, a higher fraction of voids between the shell and the powders should be expected before HIP takes place in the SS sample. These material regions are filled by the entrapped atmosphere of the L-PBF machine, which is likely to contain a higher oxygen content.

The insets in Fig. 9 a) and c) show a high-magnification SEM image of HIP SS and CP, highlighting the shell, core, and the interface between them, while Fig. 9 b) and d) report the corresponding EDS maps. The EDS analyses on large spherical particles revealed an increase in Nb content, suggesting the formation of MC carbides, as indicated by Donachie [50]. Conversely, the continuous layer surrounding the PPBs was enriched in Ti, Al and oxygen. Other literature work already highlighted the presence of MC carbides and oxides at the PPBs in the HIPed microstructure of Ni-based superalloys [47,51–53]. In particular, Qu et al. [52] reported that PPB decoration increases with a decrease in powder particle sizes. This information become particularly relevant since the present work required the usage of powders with a PSD sensibly smaller than that generally used for Near Net Shape HIP purposes. Moreover, Fox et al. [54] found that the presence of oxides along the grain boundaries can promote the nucleation of carbides from segregated areas in the alloy.

The HIP SS and CP shells developed similar microstructures with large grains coupled with twinned ones. Moreover, the images
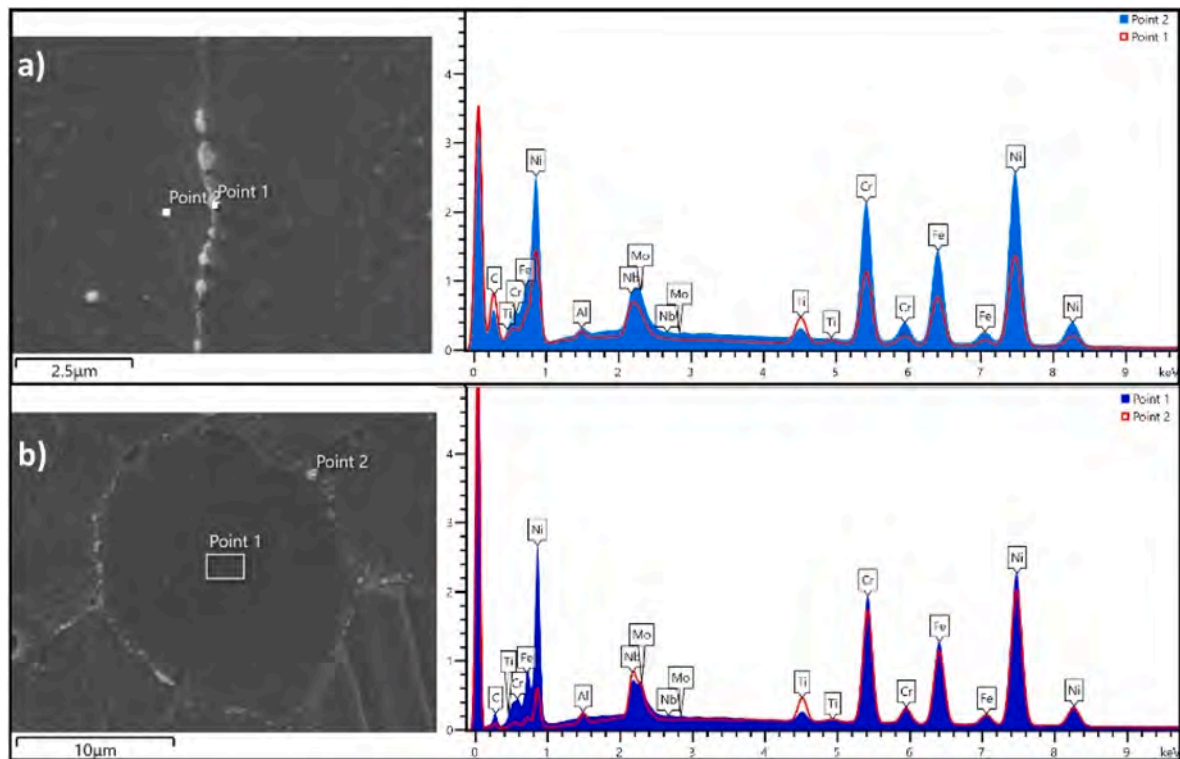
Fig. 8. EDS analysis showing the chemical nature of the precipitates located at grain a) or particle b) boundaries.
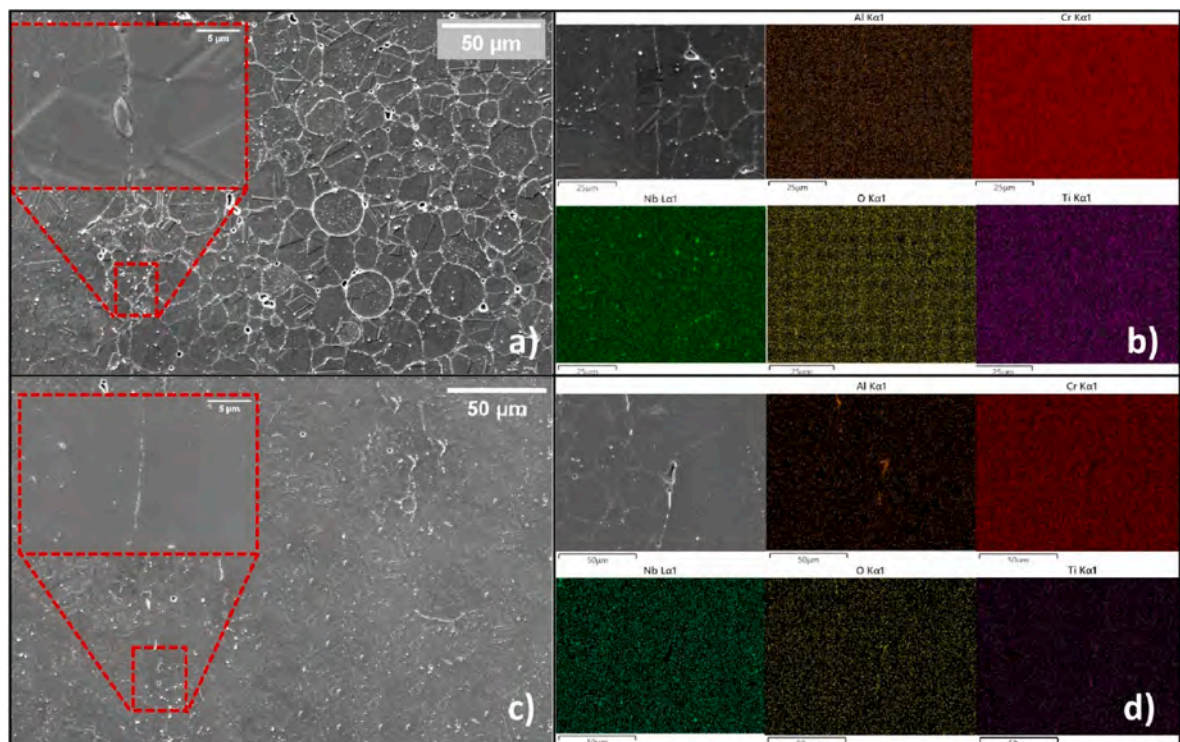
Fig. 9. High magnification SEM images and EDS analyses of HIP SS a) and b) and HIP CP c) and d).

highlighted a total dissolution of the original dendritic microstructure of the powders. This microstructure is similar to the HIP OP sample and consistent with previous literature works [48,55].

3.4. Texture e EBSD

Fig. 10 a) and b) show the Inverse Pole Figure (IPF) XO maps of HIP LP and SS.

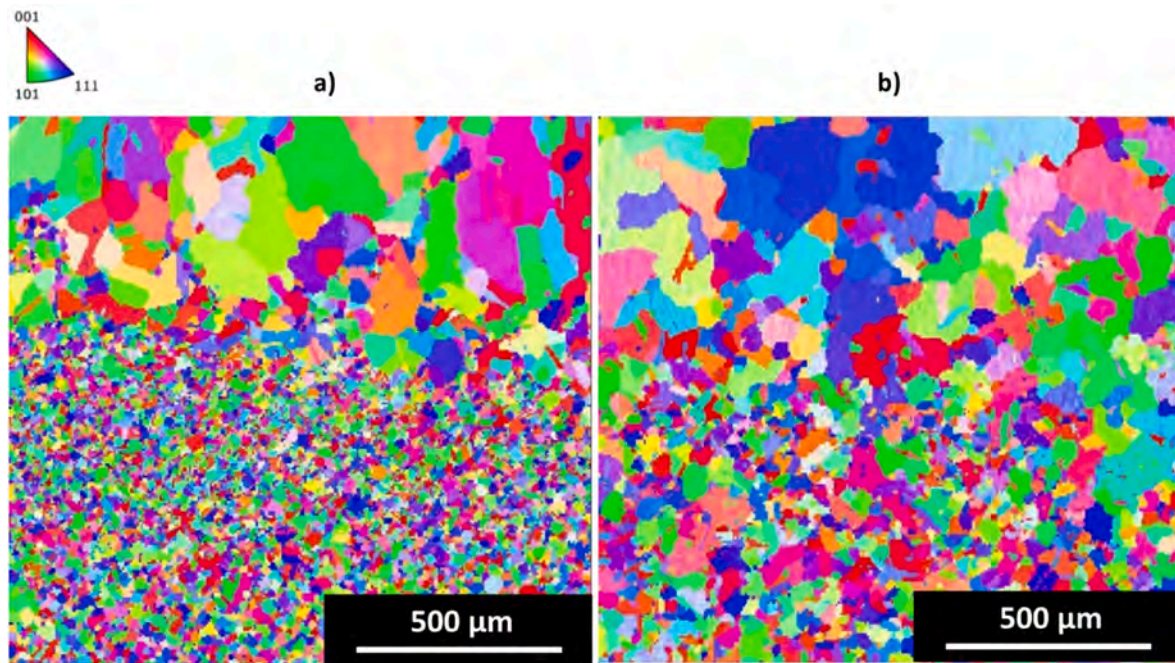A pronounced texture in either shells or cores was not observed in

Fig. 10. EBSD map of HIP SS a) and CP b).

HIP SS and CP samples. The distribution of equiaxed grains proved to be random without a preferential orientation direction. This microstructure complies with the prolonged exposure at high temperatures during the HIP process, which acted against the texturization given by the L-PBF process. This evidence aligns with other literature [55–57] investigating the AM IN718 texture evolution after HIP. Moreover, the IPF maps make the grain morphology more readable, confirming what was previously described using LOM and SEM images in paragraph 3.3.2. In particular, by analyzing the grain size measurements, a bimodal distribution was observed in HIP SS and CP, which was consistent with the previous observation.

3.5. Mechanical characterization

Microhardness and compression tests were performed to characterize the three sample families.

Hardness was investigated along the building direction for HIP SS and CP to understand grain size's influence in core-shell transition, specifically. The same test was carried out on the AB OP sample as a comparison reference value. Fig. 11 summarizes the results obtained.

The orange and yellow lines refer to the L-PBF sample in the as-built and post-HIP conditions. Since the samples were considered homogeneous, only 4 points were investigated. Conversely, the grey and blue
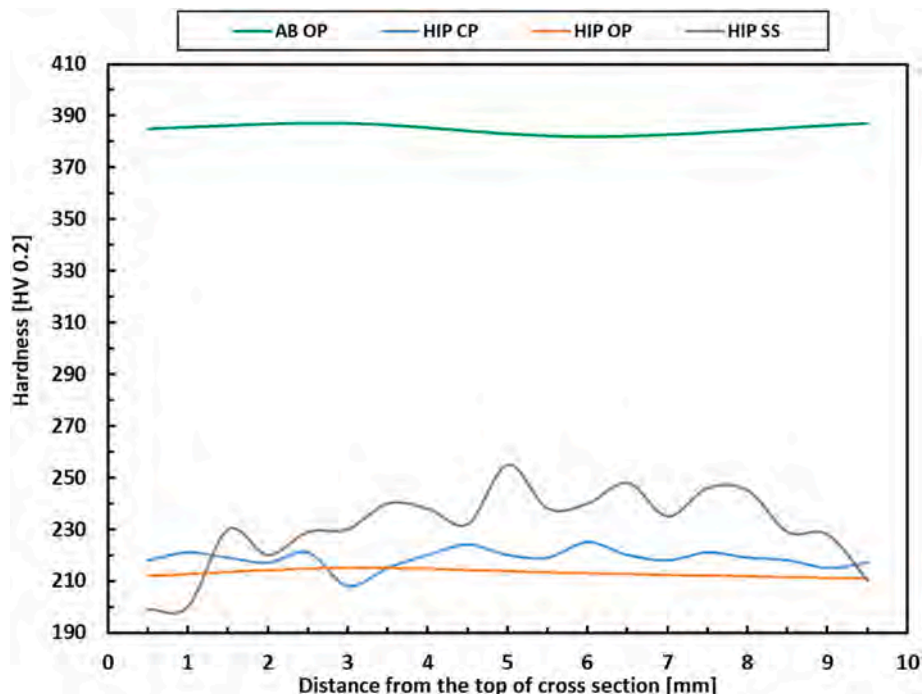

Fig. 11. Microhardness evolution of AB OP, HIP SS and CP.

lines deal with HIP CP and SS conditions, respectively, and hardness was measured with a fixed distance among imprints of 1 mm. AB OP sample showed a nearly constant HV0.2 value of 385. This high hardness value complies with the L-PBF process, where the high residual stresses and narrow dendrite structures significantly increase hardness values. Moreover, the absence of a platform preheating during the L-PBF process avoided a microstructural and property gradient along the building direction, justifying the constant values of AB OP sample. Nevertheless, the severe grain coarsening provoked by HIP treatment significantly lowered the hardness level to ca. 210 HV0.2.

HIP SS shell showed a hardness value of 210 HV0.2, which increased towards the core, where densification was achieved through sintering. The hardness span between the shell and the core was ca. 30 Hv0.2. Likewise, HIP CP shows some differences between shell and core hardness, but this time, the span between the two is limited to ca. 10 HV0.2. The larger hardness span observed in the SS sample can be explained by considering the Hall-Petch equation and the profound difference in grain size in the shell and core regions. The HV0.2 value is inversely related to the grain size, explaining the reduction observed at the shell area. The printed region with optimized parameters was utterly free of PPBs; here, the grains could freely coarse. On the other hand, inner regions were significantly populated by PPBs, which severely hindered the movement of grains. On the other hand, the CP samples only had a few PPBs and particles that could actively block the grain coarsening, thus generating an intermediate condition where grains could not grow as much as a standard L-PBF sample exposed to the same heat treatment.

Fig. 12 summarizes the results of compression tests performed on HIP OP (used as reference), HIP SS, and CP samples.

In all conditions, after a small elastic portion, a sharp increase in load is observed until the yield strength value (σ_Y) is reached. Above this value, stress and strain linearly increase with a constant rate until the machine's maximum load (100 kN) is reached. Samples underwent a severe deformation corresponding to a 53% strain. This result pointed out a good global ductility of the samples, which is typical of HIPped samples [49]. Noteworthy, the HIP OP and CP curves almost overlap, confirming the excellent densification effect of HIP in shelled CP samples. The HIP OP showed the lowest σ_Y value (361 MPa) among the conditions analyzed. HIP SS and CP samples showed σ_Y values slightly higher than HIP OP, i.e., 389 MPa and 404 MPa, respectively. These results fit with the different grain sizes corresponding to the three metallurgical conditions. HIP OP showed the coarsest microstructure, which gave the lowest yield stress in accordance with the Hall-Petch equation.
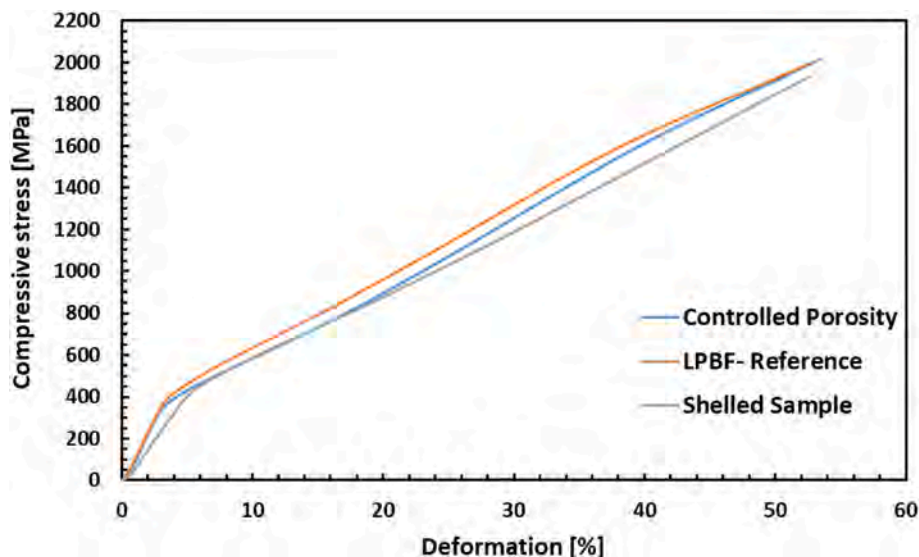
Conversely, the finer microstructure responsible for the higher yield values observed characterized the other two samples. The different grain size is responsible for altering the capability of dislocation to glide throughout the material, affecting the yield stress. The finer grain size in HIP SS and CP samples increased yield stress slightly. More specifically, HIP SS had a slightly lower yield value than the CP sample, which can be explained considering the dense presence of oxides and carbides at PPB, which are likely to limit the material ductility, especially if tensile tested [53,56].

Fig. 13 shows how the grains deformed under this severe compression test, focusing on the effect of plastic deformation in the proximity of the PPBs. This study was mainly performed to understand if the presence of such hard particles embedded in a very ductile austenitic matrix could lead to cavity formations or cracks between the two. Such behavior would indicate a low ductility attitude once the sample is under tensile load.

Fig. 13 a) shows the HIP OP sample and reveals a massive presence of deformed grains with slipping bands inside tilted by 35/40° from the load application axes. These defects occurred in low stacking fault energy material during plastic deformation [57,58] thus justifying the compression test results discussed above. Fig. 13 b) and c) reports, respectively HIP CP and SS micrographs. Compared with HIP OP, slipping bands were rarely detected in both conditions thanks to the smaller grain sizes inside cores. Globally, oxi-carbides at PPBs did not affect the grain boundary behavior during the compression test. However, Fig. 13 d) showed some interface detachment between the sintered powder of cores in HIP SS where the oxi-carbide concentration was higher. The oxide and carbide particles could act as a preferential starting point for detachments, worsening the compression behavior [53]. This outcome was totally in agreement with the evidence extrapolated by compression stress-strain curves.

4. Results discussion

Fig. 14 reports a global final comparison of the samples characterized and discussed in this work. Thanks to the geometries developed, and the scanning strategies applied, AB CP and LP underlined a valuable gain in the building time reduction compared with the bulk AB OP. This goal fits with the industrial scale-up advisable for LPBF processes.

The combination of temperature, time, and pressure during the HIP process fulfilled the expectation also under non-optimized conditions of loosened powder density (AB SS). In all the conditions investigated, a maximum of 0.04% residual porosity was detected with densification up
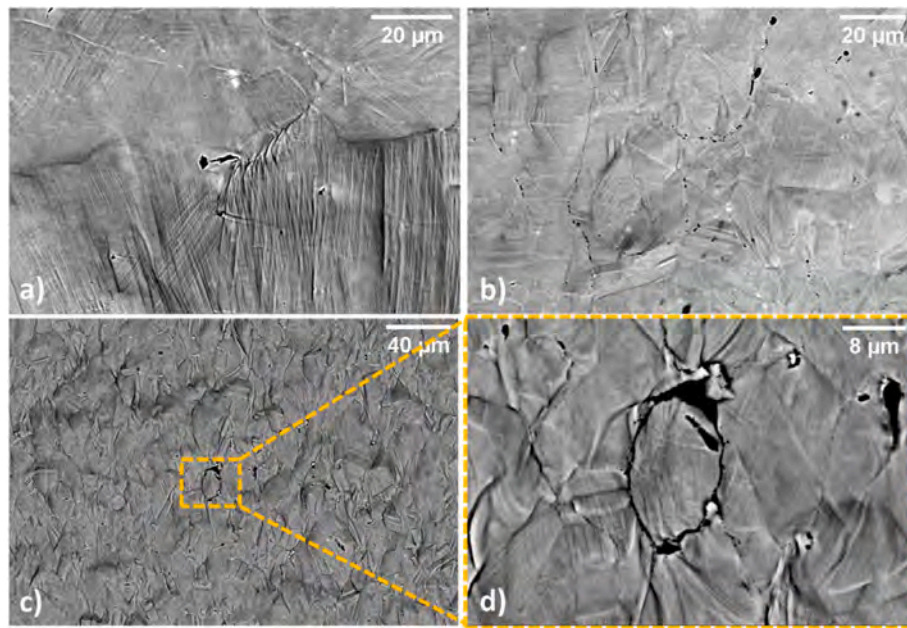

Fig. 12. HIP OP, SS, and CP stress-strain compression curves.

Fig. 13. HIP OP a), CP b), and SS c) microstructure after compression test. d) Focus on sintered particle surface detachments after the compression test.
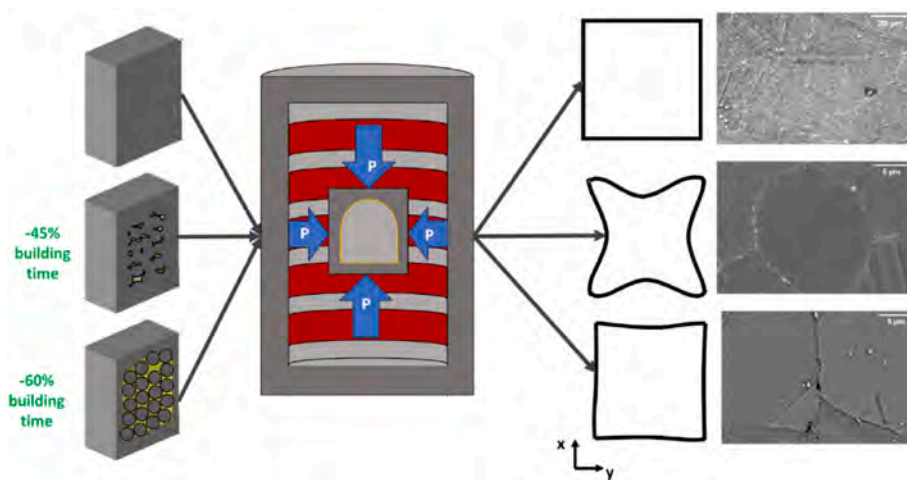

Fig. 14. Global comparison between L-PBF and HIP OP, SS, and CP samples.

to 30% (HIP SS). Despite the high densification of the HIP SS sample, a severe shrinkage was observed, an issue which could be solved only at the design stage, providing the correct geometrical tolerances. Conversely, HIP CP underwent a considerably lower shrinkage (3%), representing the most balanced condition investigated in this work.

Microstructural evolution and mechanical properties showed by the HIP CP sample were considered more promising due to its more homogeneous microstructure and hardness range between core and shell compared to the HIP SS. Moreover, this sample family behaved similarly to the reference HIP OP during the compression test, mainly because grain boundary detachment due to PPBs was not observed.

5. Conclusions

In this work, a hybrid process exploiting tailored L-PBF scanning strategy and HIP successfully obtained IN718 samples with considerable time savings. Samples produced with different strategies were investigated, and the most relevant results can be summarized as follows:

- The HIP process guaranteed high densification effects with a mean residual porosity value below 0.04% in all the conditions analyzed. The core fast melting occurred with the CP scanning strategy allowed to minimize the shrinkage effect compared to the SS scanning strategy, where the narrow powder PSD resulted in poor shape accuracy.
- HIPed shelled samples showed different microstructural evolution compared to the reference HIPed OP sample. The shelled one externally developed a coarse recrystallized microstructure similar to the reference one, while the core revealed a finer one due to high density of PPBs. The CP scanning strategy led to the formation of a more homogeneous structure with a negligible amount of PPBs. As a direct consequence of this, the difference between the core and the external surface was less evident.
- The hardness measurements were in good agreement with the microstructural observations, and in accordance with the Hall-Petch equation, all the portions where severe grain coarsening occurred showed lower hardness values. This condition is particularly evident in the HIP SS sample.

- The compression test revealed a global ductile behavior of all the HIPed samples. Nevertheless, the outcomes show potential benefits when using the controlled porosity scanning strategy instead of the loosened powder one. In particular, the negligible presence of PPBs allowed the minimization of grain boundary detachments that occurred in the SS condition.

This work demonstrated that full dense samples could be achieved by combining fast LPBF techniques and HIP; nevertheless, the limited powder size distribution of AM powder and the formation of PPBs were the most limiting factors from a geometrical and microstructural perspective when using the shelling technique. Conversely, using a faster printing strategy limited to the inner part of the sample looks promising since total deformation and precipitation of brittle phases are both extremely limited. Finally, the use of fast cooling after HIP was key towards a further post-processing time reduction.

Declaration of competing interest

The authors declare that they have no known competing financial interests or personal relationships that could have appeared to influence the work reported in this paper.

References

[1] Bassini E, Marchese G, Aversa A. Tailoring of the microstructure of laser powder bed fused inconel 718 using solution annealing and aging treatments. Metals 2021; 11:1–17. https://doi.org/10.3390/met11060921.

[2] Marchese G, Aversa A, Bassini E. Microstructure and hardness evolution of solution annealed inconel 625/tic composite processed by laser powder bed fusion. Metals 2021;11. https://doi.org/10.3390/met11060929.

[3] Frazier WE. Metal additive manufacturing: a review. J Mater Eng Perform 2014;23: 1917–28. https://doi.org/10.1007/s11665-014-0958-z.

[4] Mostafaei A, Ghiaasiaan R, Ho IT, Strayer S, Chang KC, Shamsaei N, Shao S, Paul S, Yeh AC, Tin S, To AC. Additive manufacturing of nickel-based superalloys: a state-of-the-art review on process-structure-defect-property relationship. Prog Mater Sci 2023;136:101108. https://doi.org/10.1016/J.PMATSCI.2023.101108.

[5] Kachhap K, Khandey U, Sood AK. Design for additive manufacturing for prediction of deformations and residual stresses on topologically optimised structure. Mater Today Proc 2023. https://doi.org/10.1016/J.MATPR.2023.08.245.

[6] Prathyusha ALR, Raghu Babu G. A review on additive manufacturing and topology optimization process for weight reduction studies in various industrial applications. Mater Today Proc 2022;62:109–17. https://doi.org/10.1016/J.MATPR.2022.02.604.

[7] Bassini E, Sivo A, Martelli PA, Rajczak E, Marchese G, Calignano F, Biamino S, Ugues D. Effects of the solution and first aging treatment applied to as-built and post-HIP CM247 produced via laser powder bed fusion (LPBF). J Alloys Compd 2022;905:164213. https://doi.org/10.1016/j.jallcom.2022.164213.

[8] Rigon D, Meneghetti G. Estimating the fatigue thresholds of additively manufactured metallic materials with consideration of defects. Procedia Struct Integr 2022;38:70–6. https://doi.org/10.1016/J.PROSTR.2022.03.008.

[9] Calandri M, Yin S, Aldwell B, Calignano F, Lupoi R, Ugues D. Texture and microstructural features at different length scales in Inconel 718 produced by selective laser melting. Materials 2019;12. https://doi.org/10.3390/ma12081293.

[10] Kangazian J, Shamanian M, Kermanpur A, Foroozmehr E, Badrossamay M, Sadeghi F. Characterization of the microstructure, texture, and tensile behavior of additively manufactured Hastelloy X superalloy: Insights into heat treatment at 900 °C. Mater Char 2024;208:113671. https://doi.org/10.1016/J.MATCHAR.2024.113671.

[11] Bakhshi Farkoush H, Marchese G, Bassini E, Aversa A, Biamino S. Microstructure of TiAl capsules processed by electron beam powder bed fusion followed by post-hot isostatic pressing. Materials 2023;16:5510. https://doi.org/10.3390/MA16165510.

[12] Bergman C, Skogum S. HIP-QUENCHING of aerospace parts measuring of high temperatures in a Hot isostatic press. Elsevier Science B.V.; 1994. https://doi.org/10.1016/b978-0-444-89959-0.50065-7.

[13] Raisson G, Guédou JY, Guichard D, Rongvaux JM. Production of net-shape static parts by direct HIPing of nickel base superalloy preallooyed powders. Adv Mater Res 2011;278:277–82. https://dx.doi.org/10.4028/www.scientific.net/AMR.278.277.

[14] MacDonald JE, Khan RHU, Aristizabal M, Essa KEA, Lunt MJ, Attallah MM. Influence of powder characteristics on the microstructure and mechanical properties of HIPped CM247LC Ni superalloy. Mater Des 2019;174:107796. https://doi.org/10.1016/j.matdes.2019.107796.

[15] Bampton C, Goodin W, Van Daam T, Creeger G, James S. Net shape HIP powder metallurgy components for rocket engines. HIP05 Proceedings 2005; 1-10.

[16] Kaletsch A, Qin S, Herzog S, Broeckmann C. Toughness of AM-HIP materials. 2022.

[17] He G, Liu F, Si J, Yang C, Jiang L. Characterization of hot compression behavior of a new HIPed nickel-based P/M superalloy using processing maps. Mater Des 2015; 87:256–65. https://doi.org/10.1016/j.matdes.2015.08.035.

[18] Spierings AB, Dawson K, Dumitraschkewitz P, Pogatscher S, Wegener K. Microstructure characterization of SLM-processed Al-Mg-Sc-Zr alloy in the heat treated and HIPed condition. Addit Manuf 2018;20:173–81. https://doi.org/10.1016/j.addma.2017.12.011.

[19] Sadeghi E, Karimi P, Momeni S, Seifi M, Eklund A, Andersson J. Influence of thermal post treatments on microstructure and oxidation behavior of EB-PBF manufactured Alloy 718. Mater Char 2019;150:236–51. https://doi.org/10.1016/J.MATCHAR.2019.02.016.

[20] Kaletsch A, Qin S, Herzog S, Broeckmann C. Influence of high initial porosity introduced by laser powder bed fusion on the fatigue strength of Inconel 718 after post-processing with hot isostatic pressing. Addit Manuf 2021;47:102331. https://doi.org/10.1016/J.ADDMA.2021.102331.

[21] du Plessis A, Macdonald E. Hot isostatic pressing in metal additive manufacturing: X-ray tomography reveals details of pore closure. Addit Manuf 2020;34:101191. https://doi.org/10.1016/J.ADDMA.2020.101191.

[22] du Plessis A, Razavi SMJ, Wan D, Berto F, Imdaadulah A, Beamer C, Shipley J, MacDonald E. Fatigue performance of shelled additively manufactured parts subjected to hot isostatic pressing. Addit Manuf 2022;51:102607. https://doi.org/10.1016/j.addma.2022.102607.

[23] du Plessis A, Rossouw P. Investigation of porosity changes in cast Ti6Al4V rods after hot isostatic pressing. J Mater Eng Perform 2015;24:3137–41. https://doi.org/10.1007/s11665-015-1580-4.

[24] Javadzadeh Kalahroudi F, Sadek M, Krakhmalev P, Berglund T, Bergström J, Grehk M. On the microstructure and high cycle fatigue of near-net shape PM-HIPed Inconel 625. Materials Science and Engineering: A 2023;886:145671. https://doi.org/10.1016/J.MSEA.2023.145671.

[25] Bassini E, Galech U, Soria T, Aristizabal M, Iturriza I, Biamino S, Ugues D. Effect of the particle size distribution on physical properties, composition, and quality of gas atomized Astroloy powders for HIP application. J Alloys Compd 2022;890:161631. https://doi.org/10.1016/j.jallcom.2021.161631.

[26] Kuo YL, Kakehi K. Effect of the prior particle boundary on the microstructure and mechanical properties of hot-isostatic-pressed IN718 Alloy. Mater Trans 2017;58: 1042–8. https://doi.org/10.2320/matertrans.M2017045.

[27] Chang L, Sun W, Cui Y, Yang R. Influences of hot-isostatic-pressing temperature on microstructure, tensile properties and tensile fracture mode of Inconel 718 powder compact. Mater Sci Eng 2014;599:186–95. https://doi.org/10.1016/j.msea.2014.01.095.

[28] Broeckmann C. Hot isostatic pressing of near net shape components – process fundamentals and future challenges. Powder Metall 2012;55:176–9. https://doi.org/10.1179/0032589912Z.00000000063.

[29] Sebastian R, Anke K, Christoph B. Tailor-made net-shape composite components by combining additive manufacturing and hot isostatic pressing. Hot Isostatic Pressing: HIP'17 2019;10:203–9. https://doi.org/10.21741/9781644900031-27.

[30] C. Van Nguyen, A. Bezold, C. Broeckmann, Anisotropic shrinkage of hot isostatically pressed components, (n.d.) 1–14..

[31] Kaletsch A, Qin S, Herzog S, Broeckmann C. Influence of high initial porosity introduced by laser powder bed fusion on the fatigue strength of Inconel 718 after post-processing with hot isostatic pressing. Addit Manuf 2021;47:102331. https://doi.org/10.1016/j.addma.2021.102331.

[32] Deng Y, Mirz M, Kaletsch A, Broeckmann C. Digital twin of Hot isostatic pressing technology. 2022.

[33] Du Plessis A, Yelamanchi B, Fischer C, Miller J, Beamer C, Rogers K, Cortes P, Els J, MacDonald E. Productivity enhancement of laser powder bed fusion using compensated shelled geometries and hot isostatic pressing. Advances in Industrial and Manufacturing Engineering 2021;2:100031. https://doi.org/10.1016/j.aime.2021.100031.

[34] Marchese G, Bassini E, Calandri M, Ambrosio EP, Calignano F, Lorusso M, Manfredi D, Pavese M, Biamino S, Fino P. Microstructural investigation of as-fabricated and heat-treated Inconel 625 and Inconel 718 fabricated by direct metal laser sintering: contribution of Politecnico di Torino and Istituto Italiano di Tecnologia (IIT) di Torino. 2016. https://doi.org/10.1016/j.mprp.2016.06.002. Metal Powder Report 71.

[35] Martelli PA, Sabirov I, Monclus MA, Bassini E, Marchese G, Ugues D. The effect of temperature and strain rate on the grain boundary sliding in a CM247 LC Ni-based superalloy processed with laser based powder bed fusion. J Mater Res Technol 2024;28:2466–77. https://doi.org/10.1016/J.JMRT.2023.12.131.

[36] Tillmann W, Schaak C, Nellesen J, Schaper M, Aydinöz ME, Hoyer KP. Hot isostatic pressing of IN718 components manufactured by selective laser melting. Addit Manuf 2017;13:93–102. https://doi.org/10.1016/j.addma.2016.11.006.

[37] Calandri M, Manfredi D, Calignano F, Ambrosio EP, Biamino S, Lupoi R, Ugues D. Solution treatment study of inconel 718 produced by SLM additive technique in view of the oxidation resistance. Adv Eng Mater 2018;20. https://doi.org/10.1002/adem.201800351.

[38] Jalaal M, Mehravaran K. Fragmentation of falling liquid droplets in bag breakup mode. Int J Multiphas Flow 2012;47:115–32. https://doi.org/10.1016/j.ijmultiphaseflow.2012.07.011.

[39] Tillmann W, Schaak C, Nellesen J, Schaper M, Aydinöz ME, Hoyer KP. Hot isostatic pressing of IN718 components manufactured by selective laser melting. Addit Manuf 2017;13:93–102. https://doi.org/10.1016/j.addma.2016.11.006.

[40] ElRakayby H, Kim KT. Deformation and densification behaviours of nickel-based superalloy during hot isostatic pressing. Powder Metall 2017;60:293–300. https://doi.org/10.1080/00325899.2017.1298875.

[41] Capozzi LC, Sivo A, Bassini E. Powder spreading and spreadability in the additive manufacturing of metallic materials: a critical review. J Mater Process Technol 2022;308. https://doi.org/10.1016/j.jmatprotec.2022.117706.

[42] Rao GA, Srinivas M, Sarma DS. Effect of oxygen content of powder on microstructure and mechanical properties of hot isostatically pressed superalloy Inconel 718. Mater Sci Eng 2006;435–436:84–99. https://doi.org/10.1016/j.msea.2006.07.053.

[43] Marques A, Cunha Â, Silva MR, Osendi MI, Silva FS, Carvalho Ó, Bartolomeu F. Inconel 718 produced by laser powder bed fusion: an overview of the influence of processing parameters on microstructural and mechanical properties. Int J Adv Manuf Technol 2022;121:5651–75. https://doi.org/10.1007/s00170-022-09693-0.

[44] Martucci A, Marchese G, Bassini E, Lombardi M. Effects of stress-relieving temperature on residual stresses, microstructure and mechanical behaviour of inconel 625 processed by PBF-lb/M. Metals 2023;13. https://doi.org/10.3390/met13040796.

[45] Huynh T, Mehta A, Graydon K, Woo J, Park S, Hyer H, Zhou L, Imholte DD, Woolstenhulme NE, Wachs DM, Sohn Y. Microstructural development in inconel 718 nickel-based superalloy additively manufactured by laser powder bed fusion. Metallography, Microstructure, and Analysis 2022;11:88–107. https://doi.org/10.1007/s13632-021-00811-0.

[46] Marques A, Cunha Â, Silva MR, Osendi MI, Silva FS, Carvalho Ó, Bartolomeu F. Inconel 718 produced by laser powder bed fusion: an overview of the influence of processing parameters on microstructural and mechanical properties. Int J Adv Manuf Technol 2022;121:5651–75. https://doi.org/10.1007/s00170-022-09693-0.

[47] Rezaei A, Kermanpur A, Rezaeian A, Badrossamay M, Foroozmehr E, Sadeghi F, Han J, Park TM. Contribution of hot isostatic pressing on densification, microstructure evolution, and mechanical anisotropy of additively manufactured IN718 Ni-based superalloy. Mater Sci Eng 2021;823. https://doi.org/10.1016/j.msea.2021.141721.

[48] Chandler H. Heat treater's guide: practices and procedures for nonferrous alloys. OH, USA: ASM International; 1996. n.d.

[49] Cortes J, Aristizabal M, Loretto MH, Attallah MM, Iturriza I. Effect of HIP temperature and post-HIP heat treatments on coincidence site lattices and twin boundaries in IN718, PM. World; 2016.

[50] Donachie MJ, Donachie SJ. SUPERALLOYS second edition. 2002. OH, USA.

[51] Sergi A, Khan RHU, Attallah MM. The role of powder atomisation route on the microstructure and mechanical properties of hot isostatically pressed Inconel 625. Materials Science and Engineering: A 2021;808. https://doi.org/10.1016/j.msea.2021.140950.

[52] Qu Z, Zhang P, Lai Y, Wang Q, Song J, Liang S. Influence of powder particle size on the microstructure of a hot isostatically pressed superalloy. J Mater Res Technol 2022;16:1283–92. https://doi.org/10.1016/j.jmrt.2021.12.081.

[53] Kuo YL, Kakehi K. Effect of the prior particle boundary on the microstructure and mechanical properties of hot-isostatic-pressed IN718 Alloy. Mater Trans 2017;58: 1042–8. https://doi.org/10.2320/matertrans.M2017045.

[54] S, BJW., LMHSRE Fox. Influence of carbides on the mechanical properties on inconel 718. In: Strength of metals and alloys (ICSMA 7); 1985. https://doi.org/10.1016/B978-0-08-031642-0.50004-0.

[55] Rao GA, Kumar M, Srinivas M, Sarma DS. Effect of standard heat treatment on the microstructure and mechanical properties of hot isostatically pressed superalloy inconel 718. Materials Science and Engineering: A 2003;355:114–25. https://doi.org/10.1016/S0921-5093(03)00079-0.

[56] Chang L, Sun W, Cui Y, Yang R. Preparation of hot-isostatic-pressed powder metallurgy superalloy Inconel 718 free of prior particle boundaries. Materials Science and Engineering: A 2017;682:341–4. https://doi.org/10.1016/j.msea.2016.11.031.

[57] Raabe D. Recovery and recrystallization: phenomena, physics, models, simulation. In: Physical metallurgy. fifth ed. Elsevier Inc.; 2014. p. 2291–397. https://doi.org/10.1016/B978-0-444-53770-6.00023-X.

[58] Cao Y, Bai P, Liu F, Hou X, Guo Y. Effect of the solution temperature on the precipitates and grain evolution of IN718 fabricated by laser additive manufacturing. Materials 2020;13. https://doi.org/10.3390/ma13020340.